Chapter 16
Terahertz and X-Ray Emission from Clustered Plasma and Dynamics of the Cluster Formation in the Expanding Jet

A. V. Balakin, M. S. Dzhidzhoev, V. M. Gordienko, I. A. Zhvaniya, I. E. Ivanov, N. A. Kuzechkin, P. M. Solyankin and A. P. Shkurinov

Abstract In this chapter we introduce our recent studies on terahertz (THz) and X-ray emission generated in an Ar gas-cluster jet under irradiation with high-intense ultrashort laser pulses. We carried out a numerical simulation of cluster formation

A. V. Balakin · M. S. Dzhidzhoev · V. M. Gordienko · I. A. Zhvaniya · I. E. Ivanov · N. A. Kuzechkin · P. M. Solyankin · A. P. Shkurinov (✉)
Faculty of Physics & International Laser Center, Lomonosov Moscow State University, Moscow 119991, Russia
e-mail: ashkurinov@physics.msu.ru

A. V. Balakin
e-mail: a.v.balakin@physics.msu.ru

M. S. Dzhidzhoev
e-mail: djidjoevms@mail.ru

V. M. Gordienko
e-mail: gord@phys.msu.ru

I. A. Zhvaniya
e-mail: zhvania@mail.ru

I. E. Ivanov
e-mail: ivanovmai@gmail.com

A. V. Balakin · N. A. Kuzechkin · P. M. Solyankin · A. P. Shkurinov
Institute on Laser and Information Technologies, Branch of the Federal Scientific Research Centre "Crystallography and Photonics" of Russian Academy of Sciences, Svyatoozerskaya 1, 140700 Shatura, Moscow, Russia
e-mail: lents125@mail.ru

P. M. Solyankin
e-mail: solyankin@physics.msu.ru

A. P. Shkurinov
The National University of Science and Technology MISiS, Moscow 119049, Russia

processes in a supersonic jet produced under adiabatic extension of gaseous Ar into vacuum, which shows that the concentration ratios among non-clusterized Ar monomers, small-size Ar clusters and large-size Ar clusters significantly vary along the jet. The chapter presents experimental results on THz and X-ray emission generated by irradiation of the jet with intense femtosecond laser pulses at various downstream distances measured from the nozzle outlet along the axis of symmetry of the nozzle. It is shown that THz and X-ray emission from the jet is a useful tool for the study of clustering dynamics in the course of free expansion of gas through a nozzle into vacuum.

16.1 Introduction

Over the past years the interaction of intense femtosecond laser pulses with cluster targets has been an attractive research subject because atomic and molecular clusters can couple with intense femtosecond laser pulses very efficiently and induce a range of nonlinear effects [1–8]. It is also known that a cluster beam can absorb intense ultrashort laser pulses almost completely (up to 95%) because of linear (Mie) and nonlinear resonance interactions [9, 10]. That is why, it has been regarded as a promising medium for generation of intense coherent electromagnetic pulses with sub-picosecond duration in a wide spectral range from X-ray up to THz.

The efficient emission of powerful X-ray pulses is one of the most attractive phenomena that can be observed when clusters interact with intense femtosecond laser pulses [6, 7]. When clusters are exposed to an intense femtosecond laser pulse, constituent atoms are multiply ionized, and the clusters turn into plasma with solid-state density. Because of the high local density of atoms in a cluster, which exceeds typical gas density by three orders of magnitude, part of the ions can be excited by the collision with electrons in the plasma, resulting in the emission of X-ray quanta. In a gaseous medium, the probability of electronic excitation of ions may not proceed efficiently because of the relatively low electron density. It should also be noted that the density of ions in the cluster is in general higher than that in an ionized gaseous medium. X-ray radiation from cluster plasma is comparable with X-ray yield from a solid-state target. Since the generated X-ray intensity can be dramatically increased by the clusters, their presence can be also probed by measuring the intensity of the X-ray emission.

On the other hand, it was recently found that THz radiation can be effectively generated through the interaction of a cluster medium with intense femtosecond laser pulses. Indeed, through a number of pioneering experiments, it has been revealed that THz radiation can be generated efficiently using a cluster target. It was reported [5, 11, 12] that intense THz pulses were generated when an Ar cluster beam was irradiated with femtosecond laser pulses. Nagashima et al. [5] and Jahangiri et al. [11] showed that THz pulse generation is enhanced by more than two orders of magnitude when Ar clusters are formed in an Ar cluster jet. Jahangiri et al. [11, 12] reported that the spatial distribution of emitted THz radiation from a cluster plasma exhibited a four-

lobed structure and that the dependence of the intensity of THz pulses on the laser pulse energy exhibited nonlinear growth and its quadratic increase did not show any saturation at least up to 70 mJ/pulse, which was the maximum pulse energy they were able to achieve, corresponding to the light field intensity of ~10^{17} W/cm^2. Jahangiri et al. [12] suggested that this THz radiation originates from a temporal variation of electrical quadrupoles produced by the charge separation in cluster plasma induced by a ponderomotive force of the laser pulses.

In order to understand better the processes occurring in the cluster plasma created by the irradiation of cluster jet with intense femtosecond laser pulses and to optimize the plasma formation, we need to know in detail the properties that characterize the jet such as the cluster size distribution and concentration of the clusters, the degree of condensation and the average atomic density along the beam propagation direction. This is due to the fact, that the jet formed by the adiabatic expansion of atoms (or molecules) of gas through a supersonic nozzle into vacuum, contains clusters of different sizes, as well as non-clustered atoms (or molecules) of the gas. Thus, the resulting jet is an object with significant spatial dispersion, and in this chapter, we will use the term "gas-cluster jet" when there is a need to emphasize its inherent feature. Normally, for the estimation of the mean size of the clusters produced via adiabatic expansion of gases into vacuum, a semi-empirical approach developed by Hagena [13, 14], is widely used. According to Hagena the mean cluster size $<N>$, where N represents the number of atoms in a cluster, can be estimated using the geometric dimensions of the nozzle, empirical gas constant, the stagnation pressure and the temperature of the gas in high-pressure camera. It is true that we can use the Hagena formula only for the estimation of $<N>$ and we can change $<N>$ by adjusting the stagnation pressure and the temperature of the gas flowing through the nozzle by taking advantage of the Hagena formula.

Later on, numerical simulations [15, 16] were performed for the cluster jet formation through the gas expansion from a nozzle. Moreover, a variety of experimental techniques for measuring the cluster size, such as Rayleigh scattering [15, 17, 18], optical interferometry [15–17], Raman scattering [18], and atomic beam scattering [19] were developed. It was shown that the mean cluster size and the concentration of clusters can vary significantly and non-uniformly depending on the distance from the jet axis along the radial direction [15]. This inhomogeneous distribution of clusters is certainly an important factor when we investigate the interaction of intense laser pulses with a cluster jet. For example, it was found in [20] that the position of the laser beam focus in the direction perpendicular to the symmetry axis of the nozzle is a sensitive control parameter for the X-ray generation from the laser induced plasma produced from a cluster jet. Therefore, it is expected that the distance of the laser beam focus measured from the nozzle edge along the symmetry axis of the nozzle can also be a valuable parameter to control the X-ray yield, but this has not been explored yet.

In general, the clusters' formation process in the gas jet is quite complex and is of probabilistic nature. Therefore, numerical simulations of the cluster formation processes in the free jet expansion from a nozzle could help us understand their characteristic properties. In this chapter, we introduce the results of the numerical

simulation of the formation of argon atom clusters when Ar gas passes through a supersonic conical nozzle and expands into vacuum until the jet reaches the distance of 60 mm measured from the nozzle throat along the symmetry axis of the nozzle, and demonstrates that the ratio between Ar monomers, small and large clusters fractions can change dramatically both along the jet propagation direction, and across the jet in the radial direction when the distance from the nozzle throat increases. We believe that we can take advantage of the results of this numerical simulation to optimize the yields of X-ray and THz radiation by focusing intense femtosecond laser pulses in the Ar gas-cluster jet.

16.2   Numerical Simulation of Clustering Process

The numerical simulation of condensation of Ar atoms in the supersonic conical nozzle and in the jet expanding through the nozzle was carried out taking into account the measurements of a nozzle which were used in our further experiments, its cross-section is depicted in Fig. 16.1a. The simulation was performed in two separate stages. A steady-state flow of a viscous gas in an axis-symmetric conical nozzle and in the downstream of the jet was calculated at the first stage. We solved numerically the system of two-dimensional axially symmetric non-stationary Navier-Stokes equations written in a divergent form accompanied by the ideal gas law and the boundary conditions on the edges of the computational domain. The terms responsible for convective transfer were approximated in this system by a modified Godunov scheme of high-order of accuracy [21]. The terms of the equations describing viscous diffusive transfer were approximated with the control volume scheme. The time evolution was performed by using the third-order Runge-Kutta method. It should be noted that the numerical calculation does not describe a non-stationary dynamical transition into the steady flow just after the pulsed gas beam is generated, but describes the flow of the gas beam after it becomes the steady flow.

Since the degree of expansion of the gas in the nozzle and that in the jet is sufficiently high, the gas temperature, which has a room value at the nozzle throat, rapidly drops at the nozzle output to below the critical temperature at which the clustering starts. Therefore, the temperature dependence of a viscous transfer coefficient μ was described by the modified Sutherland formula [22] as

$$\mu = \begin{cases} \mu(T_c)\left(\frac{T}{T_c}\right)^a, & T < T_c \\ \mu(T_c)\left(\frac{T}{T_c}\right)^{3/2}\frac{T_c+S}{T+S}, & T \geq T_c \end{cases} \tag{16.1}$$

where T_c represents the critical temperature of the gas, S—Sutherland constant and a—power factor. For an Ar gas, $T_c = 150$ K, $S = 128.35$ K, $a = 0.945$.

The effect of sparseness that might occur near the solid surfaces was accounted for by the boundary conditions for the velocity slip and the temperature jump at the wall of the first order [23] as

$$u_{\text{slip}} = u_s - u_{\text{wall}} = \frac{2 - \sigma}{\sigma} \lambda \frac{\partial u_s}{\partial n} + \frac{3}{4} \frac{\mu}{\rho T_G} \frac{\partial T_{\text{wall}}}{\partial s} \tag{16.2}$$

$$T_{\text{jump}} = T_G - T_{\text{wall}} = \frac{2 - \sigma_T}{\sigma_T} \frac{2\gamma}{\gamma + 1} \frac{\lambda}{\text{Pr}} \frac{\partial T_G}{\partial n}, \tag{16.3}$$

where σ is the tangential-momentum accommodation coefficient, σ_T is the thermal accommodation coefficient (for example, $\sigma = 1$ in the case of diffuse reflection from the wall with the zero tangential velocity and $\sigma = 0$ in the case of specular reflection), $\frac{\partial}{\partial n}$ and $\frac{\partial}{\partial s}$ denote the spatial derivatives in the normal and tangential directions relative to the wall, u_s is the velocity of the gas along the wall, u_{wall} is the wall velocity along the tangential direction, T_G is the temperature of the gas, T_{wall} is the wall temperature, which was fixed to be $T_{\text{wall}} = 297$ K, $\lambda = \frac{16\mu}{5\rho\sqrt{2\pi R T_G}}$ is the mean-free-path of atoms between collisions, ρ is the density of the gas, R is the specific gas constant, γ is the ratio of specific heats, and Pr is the non-dimensional Prandtl number.

At the second stage, we carried out a numerical simulation of a non-equilibrium clustering process by taking into account the previously obtained density distributions along the stream lines. A quasi-chemical model [24, 25] representing the association of a monomer to a cluster and dissociation of a monomer from a cluster was used to describe the clustering of Ar, i.e.,
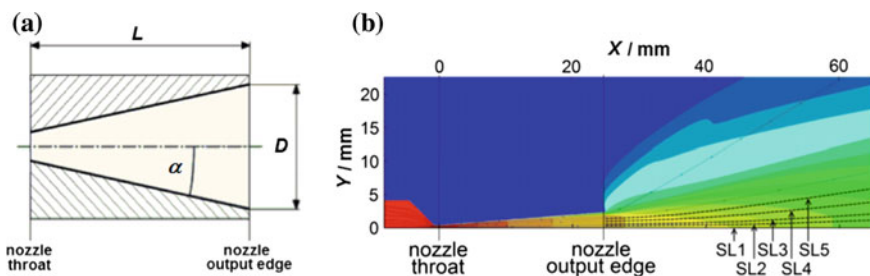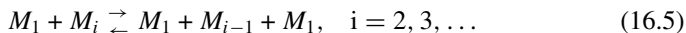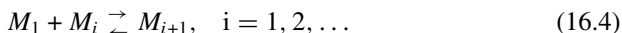
$$M_1 + M_i \underset{\leftarrow}{\overset{\rightarrow}{\rightleftarrows}} M_{i+1}, \quad i = 1, 2, \ldots \tag{16.4}$$

$$M_1 + M_i \underset{\leftarrow}{\overset{\rightarrow}{\rightleftarrows}} M_1 + M_{i-1} + M_1, \quad i = 2, 3, \ldots \tag{16.5}$$

Fig. 16.1 a Cross-section of the conical nozzle used in the experiments: $L = 24.7$ mm, $D = 4.7$ mm, $\alpha \approx 4.6°$; **b** distribution of Ar atom density inside and outside of the conical nozzle ($Y = 0$ corresponds to the axis of symmetry of the nozzle). The magnitude of the density is represented by a color scale: ~5 kg/m^3 (red), ~0.3 kg/m^3 (yellow), ~10^{-2} kg/m^3 (green), ~3×10^{-4} kg/m^3 (blue), and ~10^{-5} kg/m^3 (dark blue)

where M_1 represents a monomer and M_i represents the i-mer, which is a cluster consisting of i atoms.

An Ar vapor is considered as a mixture of perfect gases, each of which consists of i-mers. The liquid-drop model [24, 25] based on an expression for the Gibbs potential [24–26] is used for the description of the thermodynamic properties of the clusters. The Gibbs potential is given by

$$G(\rho, T, \gamma) = \sum_{i=1}^{\infty} \gamma_i G_i(p_i, T), \qquad (16.6)$$

where $G_i(p_i, T) = RT \ln(p_i / p_0) + G_i^0(T)$, p and T represent respectively the pressure and the temperature of the mixture and $p_0 = 101325$ Pa is the standard pressure. The partial pressure p_i is expressed using the molar fraction of the i-mer x_i as $p_i = px_i$, and γ_i represents the molar mass concentration of i-mer. The standard molar Gibbs potential, $G_i^0(T)$, in (16.3) is given by

$$G_i^0(T) = i G_L^0(T) + \sigma_i(T)(36\pi)^{1/3} N_A (m_1 / \rho_L(T))^{2/3} i^{2/3}, \qquad (16.7)$$

where $G_L^0(T)$ is the standard molar Gibbs potential for the liquid phase [26], $\sigma_i(T)$ is the surface tension of i-mer, $\rho_L(T)$ is the density of the liquid, N_A is the Avogadro's constant, m_1 is the mass of a monomer atom (or molecule). The standard molar Gibbs potential of $G_1^0(T)$ ($i = 1$) represents the standard molar Gibbs potential for the gaseous phase [26].

In accordance with (16.4) and (16.5), the temporal evolution of the concentrations γ_i could be described by an infinite system of the ordinary differential equations [24] as

$$\frac{d\gamma_{i+1}}{dt} = I_i - I_{i+1}, \qquad (16.8)$$

supplemented with a material balance equation given by

$$\sum_{i=1}^{\infty} i \gamma_i = \mathrm{const} = \gamma_0, \qquad (16.9)$$

where γ_0 is a given number of moles of condensing vapor molecules per kilogram in the mixture.

According to [25, 26], the specific stream of i-mer, I_i, is given by

$$I_i = \nu_{\Sigma i} \varepsilon_i \left(\frac{\gamma_i}{\varepsilon_i} - \frac{\gamma_{i+1}}{\varepsilon_{i+1}} \right), \qquad (16.10)$$

with

$$\varepsilon_i = \exp\left[-\left(\frac{G_{i+1}(p, T) - G_i(p, T)}{RT}\right)\right],$$ (16.11)

and

$$\nu_{\Sigma i} = \sum_{r=1}^{2} \nu_i^{(r)},$$ (16.12)

where $\nu_i^{(r)}$ represents the frequency of the addition of monomers to the i-mer [21, 23].

As the concentrations of i-mer and $(i+1)$-mer could differ by several orders of magnitude, we modified the system (16.5) according to [25] and also used finite-dimensional systems of N-size, obtained by truncating the original infinite system in the numerical simulation. In order to solve simultaneously the "rigid" system of the ordinary differential equations describing the kinetics of the condensation and the system of differential-algebraic equations, in which the laws of conservation of mass, momentum and energy of the mixture and the model of thermodynamics are included, we adopted an iterative computational algorithm that we developed especially for solving this problem. At each iteration step, we used the sweep method for solving the linear system with three-diagonal matrices, which were obtained by approximating the system of condensation kinetics equations according to the implicit scheme. At the same time, we solved the system of nonlinear algebraic equations, obtained from the corresponding approximations of the conservation laws and thermodynamic relations, in order to determine with high accuracy the monomer concentration and the pressure, temperature and velocity of the mixture [25].

Some of the results obtained by the numerical calculations of the cluster formation process described above are shown in Figs. 16.1b and 16.2. In the calculations, the half opening angle of the conical nozzle was set to be 4.6°, the output diameter was set to be 4.7 mm, and the nozzle length was set to be 24.7 mm, which are the same as those of the conical nozzle used in the experiment and depicted in Fig. 16.1a. The stagnation pressure of Ar gas was set to be 2 MPa. Figure 16.1b shows the spatial distribution of Ar atom density inside and outside of the conical nozzle.

The direction along the symmetry axis of the nozzle is set to be the X axis ($Y = 0$, see Fig. 16.1b), which is the same as the jet propagation direction. The nozzle throat position is set to be at the origin of the X axis, that is at $X = 0$ mm, and the nozzle output edge is placed at $X = 24.7$ mm. The radial direction, which is perpendicular to the symmetry axis of the nozzle, is denoted as the Y axis. The five stream lines, SL1-SL5, are indicated by dashed lines at Fig. 16.1b. SL1 represents the symmetry axis of the nozzle and SL2, SL3, SL4 and SL5 are the stream lines passing the spatial position at $Y = 0.4$ mm, 0.9 mm, 1.3 mm, and 1.7 mm, respectively, at $X = 24.7$ mm.

The distributions of the mean cluster size $<N>$ and mean cluster concentration $<n_{cl}>$ along the respective five stream lines as a function of the distance from the nozzle throat are shown at Fig. 16.2a and 16.2b correspondingly. The four vertical lines, CS1-CS4, show the positions of the four cross-sections located at $X =$
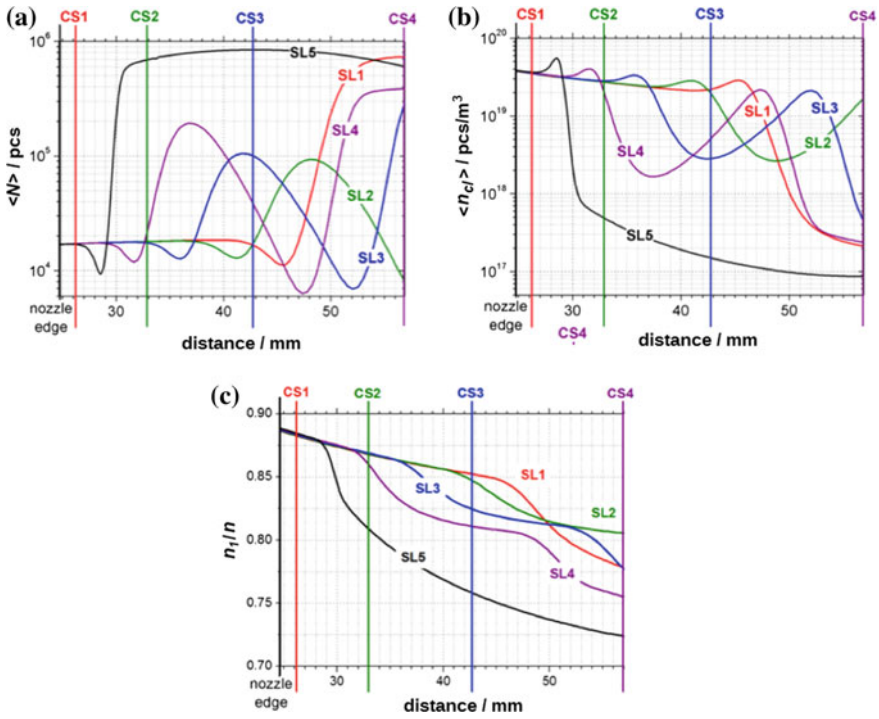
Fig. 16.2 The distribution of **a** mean cluster size $<N>$, **b** mean cluster concentration $<n_{cl}>$, and **c** ratio of monomer concentration n_1 to the total atomic concentration n along five stream lines as a function of the distance from the nozzle throat. The nozzle throat is located at $X = 0$ mm, the nozzle output edge is located at $X = 24.7$ mm (for reference see Fig. 16.1). The units of "pcs" represents the number of Ar atoms in a cluster

26.2 mm, 32.9 mm, 42.7 mm and 56.9 mm away from the nozzle throat, respectively. Accordingly, they are located downstream at 1.5 mm, 8.2 mm, 18 mm and 32.2 mm distances measured from the nozzle output edge, respectively. It is clearly seen that spatial properties of the cluster jet possesses significant dispersion in both directions both along the jet downstream and across to the propagation direction. The mean cluster size remains unchanged until SC1 cross-section and then decreases starting from the periphery of the jet, while the paraxial area of the jet still contains "frozen" size clusters up to CS2. After leaving the nozzle the mean cluster size first decreases and next significantly increases along all stream lines. Opposite to that, the mean cluster concentration first increases and then drastically decreases. This means that small-size clusters born in the vicinity of the nozzle output edge first collapse starting from the periphery toward the core of the jet and their concentration correspondingly increases, then a fast association process begins—and small clusters merge and large-size clusters appear, but their concentration consequentially drops. Also, one may note an oscillation behavior of the mean cluster size as the distance from the nozzle output edge increases along SL2, SL3, SL4.

The relative proportion of monomers in the total Ar gas atoms in the jet along five stream lines as a function of the distance from the nozzle throat is depicted at Fig. 16.2c. It can be seen that the percentage of monomers in the jet decreases when moving along the axis X from CS1 to CS4. But there are still more than 70% of monomers in SL5 even in CS4. Thus, the resulting gas-cluster jet contains not only different size clusters but plenty of non-clustered Ar atoms as well.

For better perception of the results of the numerical calculations presented at Fig. 16.2 we plotted the radial distributions of the mean cluster size and the mean cluster concentration in the cross-sections CS1, CS2, CS3 and CS4, which are depicted at Fig. 16.3a, 16.3b, 16.3c, and 16.3d, respectively. Here we denoted the radial abscissa as r to emphasize the radial symmetry of the cluster jet, and r abscissa has the same meaning as Y abscissa in Fig. 16.1b. It is clearly seen that distributions of the mean cluster size and the mean cluster concentration close to the nozzle output edge in the CS1 are homogeneous, the jet consists of small-size clusters containing around 1.8×10^4 Ar atoms each. Next three Figures: 16.3b, 16.3c, and 16.3d demonstrate the dynamics of the spatial structure of the jet along the stream.

Thus, the results of the numerical simulations presented in Figs. 16.1, 16.2 and 16.3 show that for the correct description of interaction of intense femtosecond laser pulses with the gas-cluster target one should take into account that the spatial structure of the gas-cluster jet expanding through the conical nozzle possesses significant dispersion and drastically changes both along the jet downstream and across to the
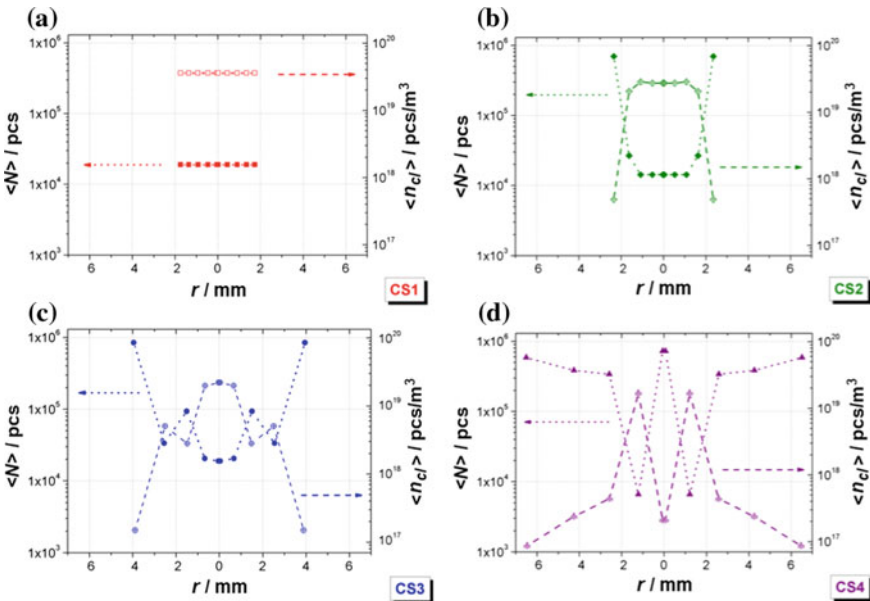

Fig. 16.3 The radial distributions of the mean cluster size and the mean concentration of clusters in the cross-sections CS1–CS4

propagation direction. So, the distance from the nozzle throat is an important parameter which defines the properties of the gas-cluster jet.

16.3 Experimental Section

16.3.1 Experimental Setup

In our experiments for the generation of THz radiation and X-ray in the cluster jet, we modified slightly the experimental setup that was described in detail in our previous report [8] so that we can irradiate the jet with a focused laser pulse at different downstream distances measured from the nozzle output edge. The focal point was located at the symmetry axis of the nozzle and could be positioned discretely along the X axis in the range between 1.5 and 32.3 mm downstream of the nozzle output edge at the locations of CS1–CS4.

Here we would like to list just the main parameters of the experimental setup. It is composed of three main modules: (i) a near-IR ultrashort laser light source generating ultrashort high-energy optical pulses, (ii) a cluster production module, and (iii) a detection system of THz and X-ray radiation. As the laser light source, we use a CPA laser system based on a femtosecond Ti:sapphire laser with a multipass amplifier, which generates pulses whose energy can be raised to 30 mJ/pulse at the repetition rate of 10 Hz. The central wavelength is 810 nm, the beam diameter is 1.5 cm, and the quality factor is $M^2 = 1.6$. The pulse duration τ can be tuned in the range between 50 fs and 600 fs by laser pulse chirping in a vacuum grating compressor. We use a conical nozzle shown at Fig. 16.1a. The nozzle is connected to a high-pressure chamber with a pulsed electromagnetic valve, which is operated at the repetition rate of 1.25 Hz and is synchronized with the laser pulse. The time delay between the laser pulse and the valve opening time was controlled using the timing module in order to optimize the temporal overlap between the laser pulse and the gas-cluster beam. We use pure argon gas for the production of Ar clusters. The maximum value of the stagnation pressure of the nozzle is set to be 2 MPa so that the background pressure in the vacuum chamber does not exceed 0.67 Pa. Other experimental details can be found in [8].

16.3.2 Experimental Results

16.3.2.1 Rayleigh Scattering

In order to verify the results obtained by the numerical simulation, we measured the Rayleigh scattering signals from the gas-cluster jet. For these Rayleigh scattering measurements, we use a continuous semiconductor laser equipped with a spatial

Fig. 16.4 The scheme of the experimental setup for the measurement of the Rayleigh scattering of laser radiation by a gas-cluster jet
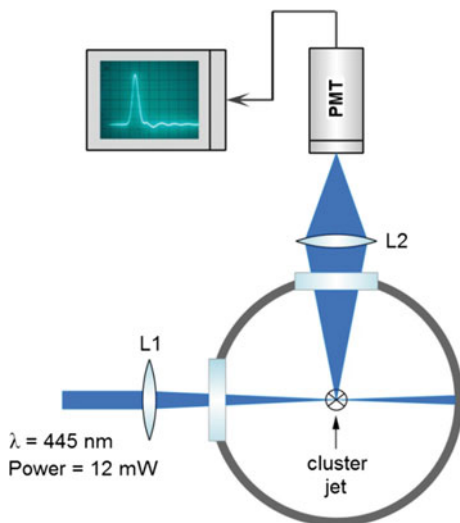
filter for the TEM$_{00}$ mode as a light source. The wavelength of the laser is 445 nm, the power is 12 mW, and the beam diameter is 1 cm. The laser light was focused on the gas-cluster jet by the L1 lens ($f = 20$ cm, 3 cmϕ), and the scattered radiation emitted in the direction perpendicular to the gas-cluster beam axis was collected through the quartz window of the vacuum chamber as shown in Fig. 16.4.

The scattered radiation was collected and focused by a lens L1 ($f = 7$ cm, 5 cmϕ) on the photomultiplier tube (PMT) detector. From the measurement of the intensity of the scattered radiation, we can estimate the average number of particles in a cluster and the volume-integrated concentration of clusters. The differential cross-section for the Rayleigh scattering by a dielectric spherical particle is given by

$$\sigma_d(\theta) = \frac{\omega^4}{c^4} \left| \frac{3}{4\pi} \frac{\varepsilon_r - 1}{\varepsilon_r + 2} \right|^2 \left(\frac{N\, m_a}{\rho} \right)^2 \sin^2(\theta), \qquad (16.13)$$

where N is the number of atoms in a cluster. The intensity of the radiation scattered by the gas-cluster jet is proportional to the $\langle N^2 \rangle \cdot \langle n_{cl} \rangle$. The squares in Fig. 16.5 represent the calculated values of the Rayleigh scattering intensities, $\langle N^2 \rangle \cdot \langle n_{cl} \rangle$, as a function of the downstream distance measured from the nozzle outlet edge. The rhombuses in Fig. 16.4 represent the observed Rayleigh scattering signal intensities. The experimental and theoretical Rayleigh scattering intensities are normalized at the distance of CS1. It can be said that the theoretical estimates reproduce the overall trend of the experimental data, even though they exhibit certain deviations from the experimental data beyond their uncertainties in the range between 2.5 and 12%.
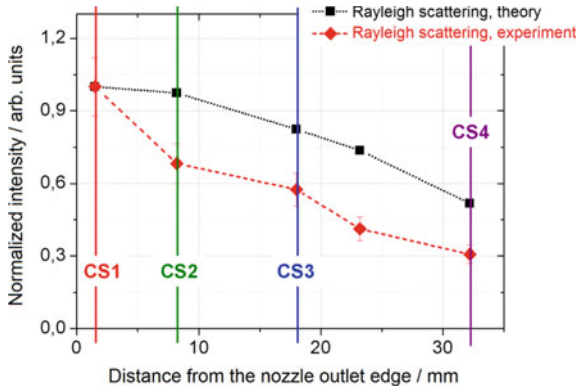
Fig. 16.5 Dependence of the Rayleigh scattering signal intensity on the downstream distance from the nozzle outlet edge. The theoretical estimates (black squares) and the experimental data (red rhombuses), both of which are normalized at CS1

16.3.2.2   Terahertz and X-Ray Emission

In our experiments THz emission generated under the single-color excitation was observed only at the angle of 30° relative to the direction of laser beam propagation. No THz signal from the Ar gas-cluster beam was registered in the forward direction. Figure 16.6 shows the dependences of the intensities of THz and X-ray pulses simultaneously generated from the Ar gas-cluster beam as a function of the laser pulse duration for both positively and negatively chirped laser pulses recorded at the three cross-sections, CS1, CS3 and CS4. The pulse duration of around 55 fs corresponds to a Fourier-limited pulse and is indicated by the central vertical dotted line in Fig. 16.6. As we mentioned above, there are mainly small-size clusters at the cross-section CS1 with the average number of atoms $<N> \approx 1.7 \times 10^4$, and cluster size distributions in cross-sections CS3 and CS4 are non-uniform: the value of $<N>$ varies from 1.6×10^4 to 8.4×10^5 in CS3 and from 8.4×10^3 to 6.0×10^5 in CS4.

As can be seen in Fig. 16.6a, the X-ray intensity takes almost the maximum value at around the minimum pulse duration and decreases as the pulse duration increases, and the maximum intensity becomes lower steadily as the distance between the excitation area and the nozzle output edge increases from CS1 to CS4. On the contrary, as can be seen in Fig. 16.6b, the THz intensity takes the lowest value at the minimum pulse duration and becomes larger as the pulse duration increases up to around 250 fs, and the THz intensities are almost the same at CS1 and CS3, and decrease largely at CS4.

The energy spectrum of the X-ray emission generated from the Ar gas-cluster beam by the single-color excitation is shown in Fig. 16.7. The presence of the gap in the energy spectrum between 3.5 and 5 keV is ascribed to the measurement procedure. The X-ray photons in the low-photon energy region below 3.5 keV where the K-line emission of Ar appears and those in the higher photon energy region above 5 keV were measured separately using different sets of filters and diaphragms which were
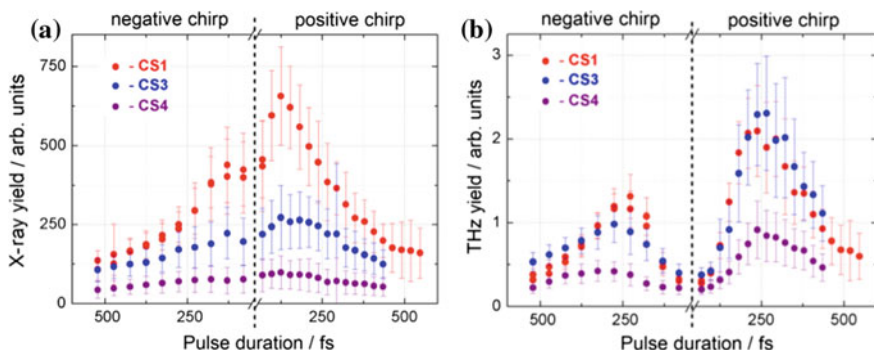
Fig. 16.6 X-Ray (**a**) and THz (**b**) yields from an Ar gas-clusters jet as a function of the temporal duration of the excitation laser pulses recorded at the cross-sections of CS1 (red dots), CS3 (blue dots), and CS4 (purple dots). The vertical dotted line in the center represents the pulse duration for a Fourier limited pulse

Fig. 16.7 Energy spectrum of the X-ray emission generated when an Ar gas cluster jet was excited at CS1 by focused negatively chirped femtosecond laser pulses (20 mJ/pulse, pulse duration of 250 fs). The backing pressure of Ar was 2 MPa

$$X\text{-}ray\ intensity \sim exp(-E/T_1),$$
$$T_1 = 1.4\ keV$$
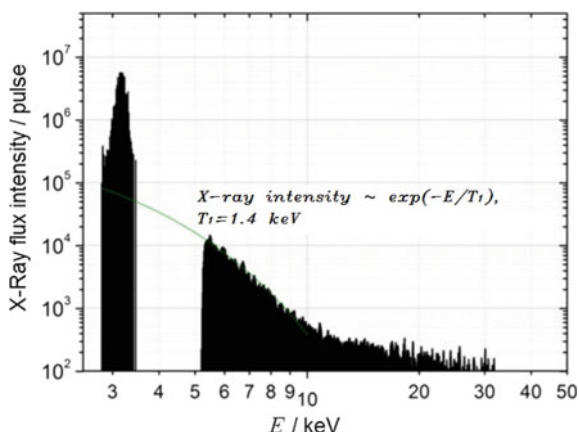
used to attenuate X-Ray intensity for achieving the single-photon counting mode of the X-ray spectrometer. It should be noted that X-ray emission generated from the Ar gas-cluster beam can be used not only for the characterization of cluster plasma itself but also for the confirmation of the formation of Ar clusters in the jet by the presence of the strong characteristic K-line of Ar in the X-ray spectrum at around 3 keV.

As long as the ponderomotive potential of electrons in the laser field exceeds the ionization potential of the K shell of Ar, the K-line X-ray can be generated efficiently from a non-clustered Ar gas. As the ponderomotive potential of electrons is given by $U_p = 9.3 \times 10^{-14} I$ (W/cm^2) $\cdot \lambda^2$ (μm^2), the ponderomotive potential in our experiment can be estimated to be $U_p = 1.8$ keV using the laser field intensity of around 3×10^{16} W/cm^2, which is smaller than 3.2 keV, the ionization potential of the K shell of Ar. This means that we could not generate the K-line X-ray using Ar

monomers. Therefore, the observation of the K-line X-ray emission shows that the dense plasma was created by the intense-field photoionization of Ar clusters, from which the K-line X-ray was generated.

The contrast ratio of K-line of Ar, i.e. the ratio of the K-line intensity with respect to the X-ray background intensity, is about 90, which is found to be higher than the contrast ratios obtained in other experimental studies [27, 28]. By approximating the energy spectrum of the continuous X-ray background by an exponential function, $\exp(-E/T_1)$, as shown in Fig. 16.7, we can estimate the mean energy T_1, which can also be called "temperature," of hot electrons as $T_1 = 1.4$ keV. Thanks to the high contrast ratio of the K-line X-ray, it was possible to record the X-ray yield online at each laser pulse using the PMT detector equipped with NaI scintillator. Therefore, the measurements of the X-ray emission to be discussed below were performed using the PMT detector for the X-ray registration. The total energy of all the X-ray quanta that reached the scintillator was recorded in each laser pulse. By taking into account the solid angle of the PMT detector and the efficiency of the X-ray generation, we estimated the number of characteristic K-line photons that was detected in each laser pulse to be 10^5. We confirmed that the X-ray yield obtained when the detection angle for the PMT detector is 45° from laser beam propagation direction and the one obtained when the detection angle is 135° are almost the same, which means that the X-ray radiation is almost isotropic.

The snapshots of the plasma channel that is formed when the Ar gas cluster jet was irradiated with femtosecond intense laser pulses are shown in Fig. 16.8. As is shown in this figure, as the distance between the laser beam focus and the nozzle output edge is increased from 1.5 to 32.3 mm, the length of the filament emitting visible light increases from 2 to 8 mm.

16.4 Discussion

It is possible that the dependences of the X-ray and THz emission yields on the laser pulse duration shown in Fig. 16.6 can be attributed to certain properties of the free electrons produced in clusters by intense femtosecond laser pulses as well as to the growth process of the clusters [29].

The maximum laser field intensity in our experiments was $I_{max} = 1.3 \times 10^{17}$ W/cm^2, which was achieved with the shortest laser pulse of about 50 fs. This light field intensity exceeds the Coulombic field within an atom. For a hydrogen atom, the intra-field at the first Bohr orbit with radius $a_B \approx 0.05$ nm is given by a well-known formula,

$$E_0 = \frac{e}{a_B^2} \approx 5 \times 10^9 (\text{V/cm}) \tag{16.14}$$

where e is the elementary charge. Consequently, the characteristic light field intensity, i.e., the characteristic energy flux density I_0 becomes

Fig. 16.8 CCD images of the plasma channel generated in the Ar gas cluster jet. The laser beam is focused at **a** CS1, **b** CS3, and **c** CS4
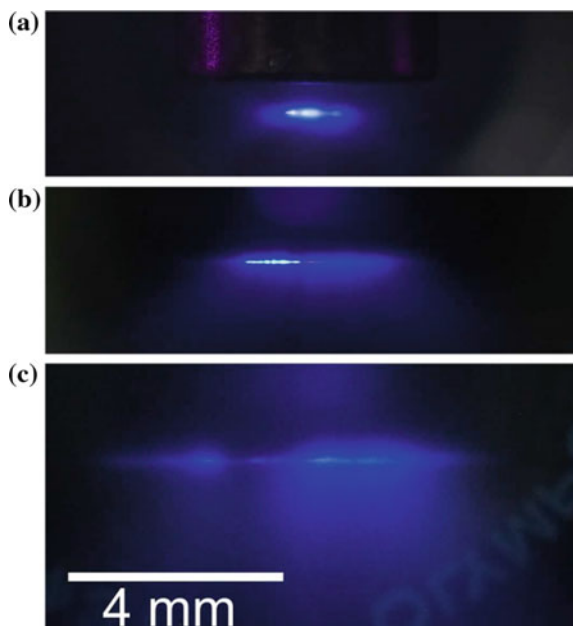
$$I_0 = \frac{cE_0^2}{8\pi} = 3.5 \cdot 10^{16} (\text{W/cm}^2). \tag{16.15}$$

At this light field intensity, the barrier-suppression ionization becomes possible, and an electron in the 1 s orbital is pulled out from a hydrogen atom by the laser field. According to the existing theoretical description of the barrier-suppression ionization of an atom [29–31], the ionization of an atom into an atomic ion having the positive charge Z occurs when the strength of the external electric field of light exceeds the critical value,

$$E_{cr} = \frac{J_Z^2}{4e^3 Z}, \tag{16.16}$$

where J_z represents the ionization potential for producing an atomic ion with the positive charge Z from an atom with the positive charge $Z - 1$. The field ionization produces free electrons with equal probability both in atoms in a cluster and in ordinary gas atoms because there are no free electrons in the cluster before the ionization and the laser field inside the cluster is not screened.

According to [32], the ionization potentials for removing the first 11 electrons in Ar are $J_1 = 15.756$, $J_2 = 27.62$, $J_3 = 40.90$, $J_4 = 59.79$, $J_5 = 75.0$, $J_6 = 91.3$, $J_7 = 123.9$, $J_8 = 143.4$, $J_9 = 422.6$, $J_{10} = 479.0$, and $J_{11} = 539.5$ eV, respectively. It can be seen that J_z increases almost 3 times from J_8 to J_9. Accordingly, the required laser field amplitude increases 7.7 times from $0.87E_0$ to $6.7E_0$, which corresponds to

the increase in the laser field intensity about 60 times from $I_8 = 2.64 \times 10^{16}$ W/cm^2 to $I_9 = 1.58 \times 10^{18}$ W/cm^2. Since the laser field intensity in our experiment did not exceed $I_{\max} = 1.3 \times 10^{17}$ W/cm^2, the ion charge Z was considered to be around 8. The chirping of the laser pulse could not change this value because $I_{\max}$ changes only by a factor of 12 in the range of the pulse duration variation in our experiment. For the first eight charge states of Ar, the ionization potential is almost proportional to Z and can be evaluated as $J_Z \sim 16.5Z$ eV. According to [29], the ionization time of these charge states can be estimated as

$$\tau_Z \sim \sqrt{2} e^2 Z \sqrt{m_e} \Big/ J_Z^{3/2} \sim 10^{16} Z^{-1} (\text{s}) \tag{16.17}$$

where *me* is the mass of an electron. This means that the ionization occurs almost immediately during the period less than one oscillation of the laser electric field.

The deeper levels with $Z \geq 9$ could be ionized through the mechanism of the impact ionization. Indeed, any free electron in the laser field with the electric field strength E and the frequency ω gains the energy W of the order of

$$W = \frac{m_e}{2} \left(\frac{eE}{m_e \omega} \right)^2 = 4300 \frac{I}{I_0} (\text{eV}), \tag{16.18}$$

which can exceed the ionization energy of the deeper levels. However, the electron impact ionization is known to take a few tens of femtoseconds in the case of atomic clusters and much longer time in the case of monomers. A cluster has high local density which is close to solid density and therefore inelastic electron-ion collisions occur quite often during the duration of the ultrashort laser pulse [33].

It is possible that the interaction of a femtosecond laser pulse with Ar clusters leads to the formation a quasi-neutral plasma inside the cluster core, and the quasi-neutrality persists during the initial stage of the laser pulse propagation. In the course of the interaction with the rising edge of the laser field, the radial distribution of the constituting atomic ions gradually becomes non-uniform with its spherical symmetry is almost being kept, but the distribution of electrons becomes asymmetric through the oscillation of electrons between the poles of the clusters [34]. The intense laser field drives electrons out of the cluster at every half period of the field oscillations, while the ion cloud gradually expands in the radial direction. Associated with the fast losses of electrons, the cluster gains a net electric charge Q. This process is the so-called outer ionization of the cluster [29] and it differs from aforementioned inner ionization when single atom inside the cluster gains a charge Z.

The effect of outer ionization is due to the different field strength in different parts of the cluster. Indeed, the total electric field affecting a single atomic ion within a cluster is composed of an external laser field averaged over a period of the laser field, the static field within the charged cluster and the dynamic field created by the oscillations of the electron cloud in the cluster driven by the laser field. On the contrary, electrons quickly respond to the variation of the electric field of the intense laser light.

In order to evaluate Q, we assume that the charge density is evenly distributed across the cluster so that the static field is radially symmetric and given by

$$E_Q(r) = \frac{Q\,r}{R^3},\tag{16.19}$$

where r is the radial distance from the center of the cluster and R is the radius of the cluster. Using the relation between the cluster charge and the laser field strength,

$$Q(R) = 4E R^2,\tag{16.20}$$

we obtain

$$E_Q(R) = 4E\tag{16.21}$$

The sum of the laser field E and cluster field E_Q has anisotropic radial distribution. Indeed, the laser field applied to the poles and cluster field E_Q are collinear to each other and their sum $E + 4E = 5E$, whereas the sum at the equator is $\sqrt{E^2 + (4E)^2} = \sqrt{17}E$, because these fields are orthogonal at the equator. It is possible that the difference between the field amplitude at the poles and the field amplitude at the equator becomes much larger by the non-uniformity of the spatial distribution of electrons. As reported in [35], the polarization-induced electric field at the poles exceeds the laser electric field by as large as one order of magnitude, which may be sufficiently large for the 9th ionization and the further ejection of electrons from Ar^{9+}. However, further calculations are needed to verify this scenario.

We can distinguish two subsystems of electrons in the cluster: the outer one, which oscillates back and forth through the cluster and the inner one, which remains inside the cluster. Energetic oscillations of the electrons from outer subsystem may lead to strong increase of electron temperature inside the cluster, which is called nonlinear resonance heating process [6]. The dependence of the X-ray yield from cluster plasma on laser pulse duration similar to that obtained in our experiments (see Fig. 16.6a), was observed in [6] and explained by the nonlinear resonance heating. The effectivity of this process is maximal at the highest intensity of laser radiation which is achieved with the shortest duration of the laser pulse.

Another process, linear resonant absorption or Mie resonance, is also possible during laser-cluster interaction [2]. After ionization by the laser field, the cluster begins to expand due to hydrodynamic forces and Coulomb pressure forces. Simplified, if we assume that the electron density inside the cluster is homogeneous, the absorption cross-section of the cluster is described by the formula:

$$\sigma_a = \frac{\pi R^3 \nu}{c} \frac{\omega_p^2/9}{(\omega - \omega_p/\sqrt{3})^2 + \nu^2/4}\tag{16.22}$$

At a certain moment during expansion, when the condition $\omega = \omega_p \big/ \sqrt{3}$ is reached, laser pulse energy is resonantly absorbed by the cluster. Linear resonance absorption leads to increase of the number of electrons in the inner subsystem of the cluster. We assume that the dependence of THz intensity on laser pulse duration presented in Fig. 16.6b can be explained by the effect of linear resonance absorption.

By following the discussion in [12], we assume that the THz radiation produced by the laser radiation is generated by a time-varying axially symmetric linear quadrupole, which is produced by the ponderomotive force of the laser pulse. Indeed, because of the ponderomotive force, the plasma filament produced by the laser pulse expands radially first, and then, shrinks back after the propagation of the laser pulse, resulting in the formation of the time-varying linear quadrupole.

The decrease in the X-ray emission yield as the distance X between the nozzle output edge and the laser focus increases from CS1 to CS4 may be ascribed to the characteristic propagation of the intense laser pulse in an Ar gas-cluster jet. As the distance X increases, the length of the interaction region increases and the density of clusters in the laser excitation volume decreases. Furthermore, because the laser beam can be defocused by the free electrons formed by the ionization of Ar monomers in the Ar gas-cluster jet, the laser radiation could interact with clusters less efficiently.

As shown in [5], the waveform of the pulsed THz radiation comprises two half-periods corresponding to the one-time radial expansion and subsequent compression of the filament. A phenomenological model of the THz radiation developed in [12] takes into account the effect of the finite length L of the filament, which is larger than the wavelength λ of the THz radiation. It was shown in [12] that the transition radiation and Cherenkov radiation could not explain the experimental angular distribution of THz radiation generated from the plasma produced from a gas-cluster jet. A mechanism of low-frequency quadrupole emission from a plasma channel, which is created by femtosecond laser pulse in gaseous medium, was studied theoretically in [36]. The interference of quadrupole THz sources in the plasma channel results in the formation of a specific angular distribution of the THz field, which takes a minimal value along the filament axis and a maximum value at the angle $\theta_{\max}$ between the detector and the filament axis given by

$$\theta_{\max} = 69° \sqrt{L / \lambda} \tag{16.23}$$

In our present experiments, the THz radiation was collected at the deflection angle of 30° from the laser propagation direction. The laser beam is focused at different downstream distances from the nozzle output edge and the length of the filament should vary, so the angular distribution of the THz radiation is expected to change. In accordance with formula (16.23) we expect a decrease of $\theta_{\max}$ when X increases, since the value of L grows (see Fig. 16.8).

16.5 Conclusion

We have carried out numerical simulations of the cluster formation process in a supersonic jet of Ar, and found that the spatial distribution of the cluster concentration represents the clustering dynamics in the jet expansion. We have shown that the distance from the nozzle output edge along the symmetry axis of a cylindrical nozzle is an important parameter describing the properties of the cluster target.

We have shown that the difference in the optimal laser pulse duration for the efficient generation of X-ray and that for the efficient generation of THz radiation can be explained by the different time periods required for the formation of electron subsystems in an Ar cluster. The population of the outer electrons increases quickly during the first 50 fs and they are responsible for the generation of X-ray, which explains the maximum X-ray yield at the minimal pulse duration in our experiments. The number of inner electrons increases only slowly and reaches maximum at the time scale of the order of 100 fs, which can be attributed to the enhancement of THz yield at $\tau \approx 250$ fs in our experiments. At the later stage, the number of the outer electrons begins to rise again, which may decrease the intensity of the THz radiation.

References

1. T. Ditmire, T. Donnelly, A.M. Rubenchik, R.W. Falcone, M.D. Perry, Interaction of intense laser pulses with atomic clusters. Phys. Rev. A Gen. Phys. **53**, 3379 (1996)
2. T.D. Donnelly, T. Ditmire, K. Neuman, M.D. Perry, R.W. Falcone, High-order harmonic generation in atom clusters. Phys. Rev. Lett. **76**, 2472 (1996)
3. I. Alexeev, T.M. Antonsen, K.Y. Kim, H.M. Milchberg, Self-focusing of intense laser pulses in a clustered gas. Phys. Rev. Lett. **90**, 103402 (2003)
4. P.K. Tiwari, V.K. Tripathi, Stimulated raman scattering of a laser in a plasma with clusters. Phys. Plasmas **11**, 1674 (2004)
5. T. Nagashima, H. Hirayama, K. Shibuya, M. Hangyo, M. Hashida, S. Tokita, S. Sakabe, Terahertz pulse radiation from argon clusters irradiated with intense femtosecond laser pulses. Opt. Exp. **17**, 8907 (2009)
6. L.M. Chen, F. Liu, W.M. Wang, M. Kando, J.Y. Mao, L. Zhang, J.L. Ma, Y.T. Li, S.V. Bulanov, T. Tajima, Y. Kato, Z.M. Sheng, Z.Y. Wei, J. Zhang, Intense high-contrast femtosecond K-shell x-ray source from laser-driven Ar clusters. Phys. Rev. Lett. **104**, 215004 (2010)
7. V.M. Gordienko, M.S. Dzhidzhoev, I.A. Zhvaniya, V.T. Platonenko, D.N. Trubnikov, D.O. Fedorov, Hard X-ray generation and plasma filament formation under interaction of femtosecond laser pulses with large molecular clusters. Eur. Phys. J. D **67**, 55 (2013)

8. A.V. Balakin, M.S. Dzhidzhoev, V.M. Gordienko, M.N. Esaulkov, I.A. Zhvaniya, K.A. Ivanov, I.A. Kotelnikov, N.A. Kuzechkin, I.A. Ozheredov, V.Y. Panchenko, A.B. Savel'ev, M.B. Smirnov, P.M. Solyankin, A.P. Shkurinov, IEEE Trans. Terahertz Sci. Technol. **7**, 79 (2017)

9. M. Kundu, D. Bauer, Optimizing the ionization and energy absorption of laser-irradiated clusters. Phys. Plasmas **15**, 033303 (2008)

10. T. Ditmire, R.A. Smith, J.W.G. Tisch, M.H.R. Hutchinson, High intensity laser absorption by gases of atomic clusters. Phys. Rev. Lett. **78**, 3121 (1997)

11. F. Jahangiri, M. Hashida, T. Nagashima, S. Tokita, M. Hangyo, S. Sakabe, Intense terahertz emission from atomic cluster plasma produced by intense femtosecond laser pulses. Appl. Phys. Lett. **99**, 261503 (2011)

12. F. Jahangiri, M. Hashida, S. Tokita, T. Nagashima, M. Hangyo, S. Sakabe, Enhancing the energy of terahertz radiation from plasma produced by intense femtosecond laser pulses. Appl. Phys. Lett. **102**, 191106 (2013)

13. O.F. Hagena, W. Obert, Cluster formation in expanding supersonic jets: effect of pressure, temperature, nozzle size, and test gas. J. Chem. Phys. **56**, 1793 (1972)

14. O.F. Hagena, Cluster ion sources. Sci. Instrum. **63**, 2374 (1992)

15. F. Dorchies, F. Blasco, T. Caillaud, J. Stevefelt, C. Stenz, A.S. Boldarev, V.A. Gasilov, Spatial distribution of cluster size and density in supersonic jets as targets for intense laser pulses. Phys. Rev. A **68**, 023201 (2003)

16. F. Blasco, T. Caillaud, F. Dorchies, C. Stenz, J. Stevefelt, A.S. Boldarev, V.A. Gasilov, Characterization of argon cluster jets for laser interaction studies. Nucl. Instr. Meth. Phys. Res. B **205**, 324 (2003)

17. K.Y. Kim, V. Kumarappan, H.M. Milchberg, Measurement of the average size and density of clusters in a gas jet. Appl. Phys. Lett. **83**, 3210 (2003)

18. A. Ramos, J.M. Fernández, G. Tejeda, S. Montero, Quantitative study of cluster growth in free-jet expansions of CO_2 by Rayleigh and Raman scattering. Phys. Rev. A **72**, 053204 (2005)

19. U. Buck, R. Krohne, Cluster size determination from diffractive He atom scattering. J. Chem. Phys. **105**, 5408 (1996)

20. J.-Y. Lin, H. Chu, M. Shen, Y. Xiao, C.-H. Lee, S. Chen, J. Wang, Opt. Commun. **231**, 375 (2004)

21. G.S. Glushko, I.E. Ivanov, I.A. Kryukov, Math. Model. Comput. Simul. **2**, 407 (2010)

22. D.Y. Dubov, *Proceedings of All-Russian Conference Contemporary Problems of Rarefied Gas Dynamics* (2013)

23. S. Roy, R. Raju, H.F. Chuang, B.A. Cruden, M. Meyyappan, J. Appl. Phys. **93**, 4870 (2003)

24. Y.A. Ryzhov, U.G. Pirumov, V.N. Gorbunov, *Nonequilibrium condensation in high-speed gas flows* (Gordon and Breach Science Publishers, Philadelphia, 1989)

25. V.A. Volkov, A.V. Muslaev, U.G. Pirumov, P.V. Rozovskii, Fluid Dyn. **30**, 399 (1995)

26. L.V. Gurvich, I.V. Veiz, V.A. Medvedev, *Thermodynamic Properties of Individual Substances*, Book 2, vol. 4 (Moscow, Nauka, 1981)

27. L.M. Chen, M. Kando, J. Ma, H. Kotaki, Y. Fukuda, Y. Hayashi, I. Daito, T. Homma, K. Ogura, M. Mori, A.S. Pirozhkov, J. Koga, H. Daido, S.V. Bulanov, T. Kimura, T. Tajima, Y. Kato, Phase-contrast x-ray imaging with intense Ar Kα radiation from femtosecond-laser-driven gas target. Appl. Phys. Lett. **90**, 211501 (2007)

28. L. Zhang, L.-M. Chen, D.-W. Yuan, W.-C. Yan, Z.-H. Wang, C. Liu, Z.-W. Shen, A. Faenov, T. Pikuz, I. Skobelev, V. Gasilov, A. Boldarev, J.-Y. Mao, Y.-T. Li, Q.-L. Dong, X. Lu, J.-L. Ma, W.-M. Wang, Z.-M. Sheng, J. Zhang, Enhanced Kα output of Ar and Kr using size optimized cluster target irradiated by high-contrast laser pulses. Opt. Exp. **19**, 25812 (2011)

29. V. Krainov, M. Smirnov, Cluster beams in the super-intense femtosecond laser pulse. Phys. Rep. **370**, 237 (2002)

30. V.P. Krainov, B.M. Smirnov, M.B. Smirnov, Femtosecond excitation of cluster beams. Phys. Usp. **50**, 907 (2007)

31. N.B. Delone, V.P. Krainov, Tunneling and barrier-suppression ionization of atoms and ions in a laser radiation field. Phys. Usp. **41**, 469 (1998)

32. I.K. Kikoin, *Tables of Physical Quantities (Handbook)* (Atomizdat, Moscow, 1976). (in Russian)
33. B.M. Smirnov, Cluster plasma. Phys. Usp. **43**, 453 (2000)
34. Y. Fukuda, Y. Kishimoto, T. Masaki, K. Yamakawa, Structure and dynamics of cluster plasmas created by ultrashort intense laser fields. Phys. Rev. A **73**, 031201 (2006)
35. C. Jungreuthmayer, M. Geissler, J. Zanghellini, T. Brabec, Microscopic analysis of large-cluster explosion in intense laser fields. Phys. Rev. Lett. **92**, 133401 (2004)
36. N.A. Panov, O.G. Kosareva, V.A. Andreeva, A.B. Savel'ev, D.S. Uryupina, R.V. Volkov, V.A. Makarov, A.P. Shkurinov, JETP. Lett. **93**, 638 (2011)